Cryo–electron tomography reveals a critical role of RIM1α in synaptic vesicle tethering

Rubén Fernández-Busnadiego,[1] Shoh Asano,[1] Ana-Maria Oprisoreanu,[2,3] Eri Sakata,[1] Michael Doengi,[4] Zdravko Kochovski,[1] Magdalena Zürner,[2,3] Valentin Stein,[4] Susanne Schoch,[2,3] Wolfgang Baumeister,[1] and Vladan Lučić[1]

[1]Department of Molecular Structural Biology, Max Planck Institute of Biochemistry, 82152 Martinsried, Germany
[2]Department of Neuropathology, [3]Department of Epileptology, and [4]Institute of Physiology II, University of Bonn, 53105 Bonn, Germany

Synaptic vesicles are embedded in a complex filamentous network at the presynaptic terminal. Before fusion, vesicles are linked to the active zone (AZ) by short filaments (tethers). The identity of the molecules that form and regulate tethers remains unknown, but Rab3-interacting molecule (RIM) is a prominent candidate, given its central role in AZ organization. In this paper, we analyzed presynaptic architecture of RIM1α knockout (KO) mice by cryo–electron tomography. In stark contrast to previous work on dehydrated, chemically fixed samples, our data show significant alterations in vesicle distribution and AZ tethering that could provide a structural basis for the functional deficits of RIM1α KO synapses. Proteasome inhibition reversed these structural defects, suggesting a functional recovery confirmed by electrophysiological recordings. Altogether, our results not only point to the ubiquitin–proteasome system as an important regulator of presynaptic architecture and function but also show that the tethering machinery plays a critical role in exocytosis, converging into a structural model of synaptic vesicle priming by RIM1α.

Introduction

Presynaptic terminals are axonal specializations in which synaptic vesicles are exocytosed in response to membrane depolarization-induced Ca^{2+} influx. The high speed of synaptic transmission relies on a subset of "primed" vesicles that fuse within few milliseconds upon Ca^{2+} influx, the so-called readily releasable pool (RRP; Südhof, 2004). Vesicle fusion takes place at the active zone (AZ), a specialized section of the presynaptic membrane directly opposed to the postsynaptic density. The close association of primed vesicles to the AZ, a prerequisite for rapid fusion, is mediated by a dense network of proteins known as the presynaptic cytomatrix (Schoch and Gundelfinger, 2006).

3D EM techniques have revealed the filamentous nature of the presynaptic cytomatrix (Landis et al., 1988; Hirokawa et al., 1989; Siksou et al., 2007, 2009). However, these studies were performed in dehydrated samples that may suffer structural alterations (Dubochet and Sartori Blanc, 2001). Cryo–electron tomography (cryo-ET) allows 3D visualization at molecular resolution of fully hydrated biological structures optimally preserved by vitrification (Dubochet et al., 1988; Vanhecke et al., 2011). Furthermore, cryo-ET requires no heavy metal staining, and therefore, biomolecules are visualized directly. On the other hand, frozen-hydrated samples are more sensitive to radiation damage than their plastic-embedded counterparts, which imposes low electron dose imaging conditions resulting in higher noise levels. Also, the difficulties associated with thinning frozen-hydrated material often restrict sample choice to inherently thin specimens. We have recently used cryo-ET to show that in unstained, vitrified frozen-hydrated mammalian synapses the presynaptic cytomatrix mainly consists of filaments shorter than 40 nm linking vesicles to each other (connectors) or to the AZ (tethers; Fernández-Busnadiego et al., 2010).

Currently, the identity of the proteins forming and regulating those filaments is unknown. Our previous results (Fernández-Busnadiego et al., 2010) led to a model in which vesicles are

R. Fernández-Busnadiego and S. Asano contributed equally to this paper.

Correspondence to Vladan Lučić: vladan@biochem.mpg.de

R. Fernández-Busnadiego's present address is Dept. of Cell Biology, Yale University School of Medicine, New Haven, CT 06510.

E. Sakata's present address is Dept. of Molecular Biophysics and Biochemistry, Yale University School of Medicine, New Haven, CT 06510.

Abbreviations used in this paper: ACSF, artificial cerebrospinal fluid; AMC, 7-amino-4-methylcoumarin; AZ, active zone; cryo-ET, cryo–electron tomography; fEPSP, field excitatory postsynaptic potential; HB, homogenization buffer; HBM, Hepes-buffered medium; KO, knockout; K-W, Kruskal-Wallis; PPF, paired-pulse facilitation; RIM, Rab3-interacting molecule; RRP, readily releasable pool; UPS, ubiquitin–proteasome system; WT, wild type.

© 2013 Fernández-Busnadiego et al. This article is distributed under the terms of an Attribution–Noncommercial–Share Alike–No Mirror Sites license for the first six months after the publication date (see http://www.rupress.org/terms). After six months it is available under a Creative Commons License (Attribution–Noncommercial–Share Alike 3.0 Unported license, as described at http://creativecommons.org/licenses/by-nc-sa/3.0/).

The Rockefeller University Press $30.00
J. Cell Biol. Vol. 201 No. 5 725–740
www.jcb.org/cgi/doi/10.1083/jcb.201206063

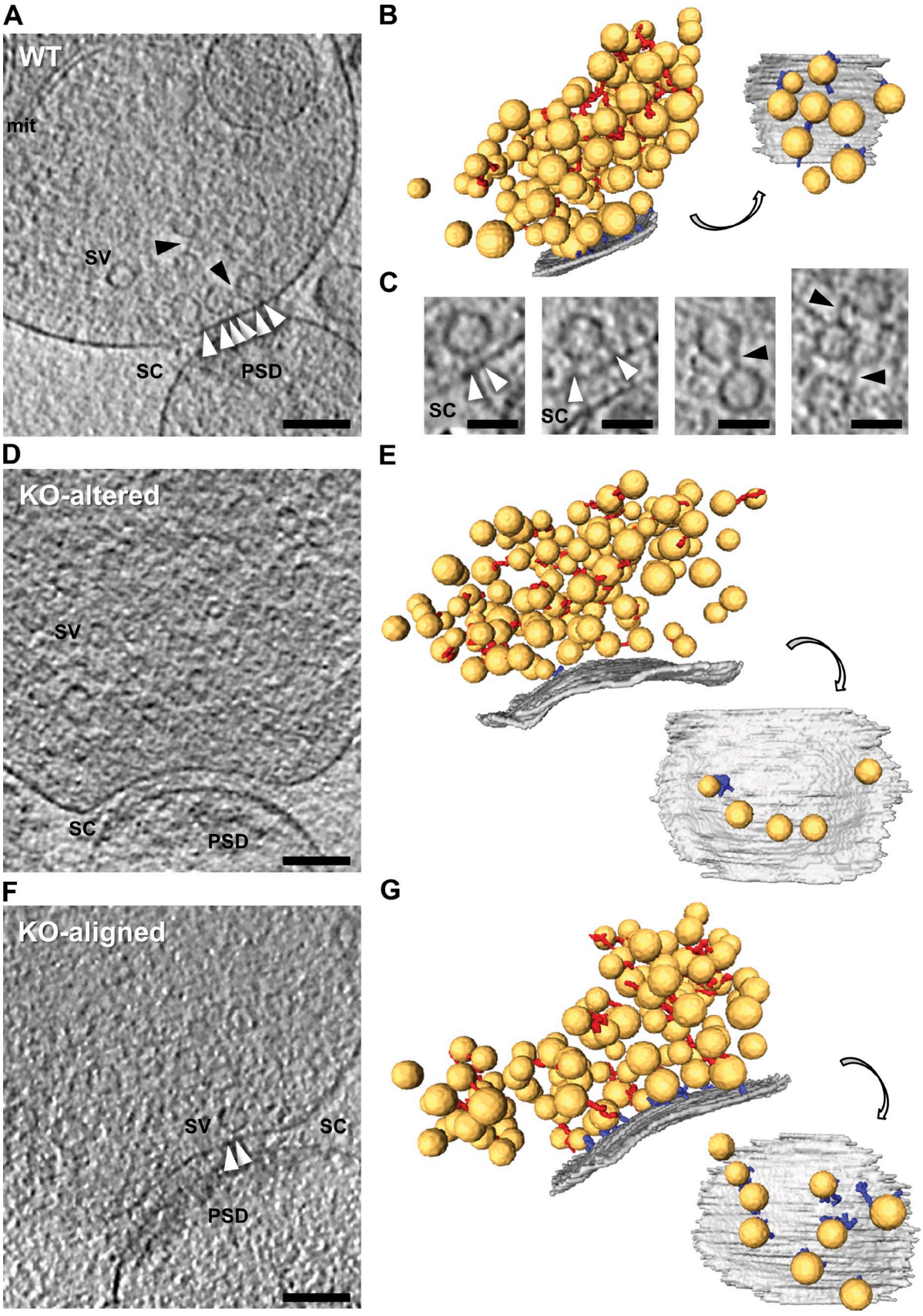

Figure 1. **Morphology of WT and RIM1α KO synapses by cryo-ET.** In unstained, vitrified frozen-hydrated mammalian synapses, the presynaptic cytomatrix mainly consists of filaments shorter than 40 nm linking vesicles to each other (connectors) or to the AZ (tethers). (A, D and F) Tomographic slices of WT (A), RIM1α KO-altered (D), and RIM1α KO-aligned (F) synapses. mit, mitochondrion; PSD, postsynaptic density; SC, synaptic cleft; SV, synaptic vesicle.

first captured at the AZ by one or few tethers. Once in the vicinity of the AZ, vesicles acquire additional, shorter tethers most likely in a SNARE-dependent manner. The distance between vesicles and the AZ is reduced with increasing number of tethers, which has been shown to facilitate fusion (Li et al., 2007; van den Bogaart et al., 2011). Thus, vesicles with multiple short tethers are structurally primed and ready for fusion upon Ca^{2+} influx.

In addition to SNAREs, other AZ proteins may be involved in tether formation. Rab3-interacting molecule (RIM) is a prominent candidate because of its central role in AZ organization, as it interacts with Ca^{2+} channels, synaptic vesicle proteins, and most other AZ-enriched proteins (Mittelstaedt et al., 2010; Jahn and Fasshauer, 2012; Südhof, 2012). Recent work has demonstrated that RIM promotes vesicle priming by reversing MUNC13 homodimerization (Deng et al., 2011) and that RIM is necessary to recruit Ca^{2+} channels and anchor vesicles to the AZ (Han et al., 2011; Kaeser et al., 2011).

Seven RIM isoforms (with multiple splice variants) are present in the brain. RIM1α, the most abundant isoform, is particularly interesting because RIM1α knockout (KO) mice suffer severe deficits in synaptic transmission, memory, and learning (Powell et al., 2004), a higher propensity for epileptic seizures (Pitsch et al., 2012), and schizophrenia-like behavioral features (Blundell et al., 2010). Hippocampal slices of RIM1α KO mice showed a large reduction in release probability in excitatory (Schoch et al., 2002) and inhibitory synapses (Kaeser et al., 2008), whereas autapses (synapses made by a neuron onto itself) exhibited a decrease in the RRP (Calakos et al., 2004). Synapses from other brain areas also showed impaired transmission (Mittelstaedt et al., 2010). However, no obvious structural phenotype was observed in chemically fixed, dehydrated, and heavy metal–stained synapses from RIM1α KO or RIM1α/2α double KO mice (Schoch et al., 2002, 2006).

Recent work has shown that the ubiquitin–proteasome system (UPS) homeostatically regulates RIM levels in a terminal-specific manner, correlating presynaptic RIM levels with synaptic activity (Yao et al., 2007; Jiang et al., 2010; Lazarevic et al., 2011). Those studies showed as well that other presynaptic proteins, such as MUNC13 or synapsin, are also UPS targets. Thus, beyond the well-characterized roles of the UPS in postsynaptic function and neurodegenerative pathology (Bingol and Sheng, 2011), the UPS is emerging as an important regulator of presynaptic function.

Here, we investigated presynaptic architecture in synaptosomes obtained from RIM1α KO brains using cryo-ET. Synaptosomes are a widely established model for neurotransmitter release that can sustain multiple exocytic cycles (Whittaker, 1993; Nicholls, 2003). Although some aspects of synaptic transmission are likely perturbed in synaptosomes, we previously showed that presynaptic terminals from synaptosomes and organotypic slices are comparable in terms of vesicle number and distribution and presynaptic cytomatrix organization (Fernández-Busnadiego et al., 2010). Also, in both preparations, long actin filaments are common postsynaptically but not in presynaptic terminals. Synaptosomes are currently the only preparation allowing the cryo-ET study of presynaptic architecture with sufficient throughput, as accessing synapses in organotypic slices or dissociated cultures often requires thinning procedures with extremely low yield (Fernández-Busnadiego et al., 2011). This study focuses on RIM1α KO synapses given that RIM1α is the preponderant RIM isoform and that deletion of further RIMs causes lethality (Kaeser et al., 2008; Mittelstaedt et al., 2010), thus hindering synaptosome extraction. To analyze the structural role of the UPS in the presynaptic terminal, we have studied wild-type (WT) and KO synapses in the presence of the proteasome inhibitor MG132. We have quantitatively analyzed tomograms using previously developed software providing objective and comprehensive detection and analysis of connectors and tethers (see Materials and methods; Fernández-Busnadiego et al., 2010), as automated data analysis is particularly necessary to extract the features of interest within crowded environments such as the AZ.

Our results reveal prominent reductions in vesicle tethering and vesicle concentration at the AZ of RIM1α KO synapses that could provide a structural basis for the functional deficits observed in those terminals. By means of cryo-ET and electrophysiological recordings, we show that proteasome inhibition reversed those structural defects and increased release probability to WT levels. Proteasome inhibition also induced a significant increase in vesicle connectivity and vesicle diameter in both WT and KO synapses. Thus, our data point to the UPS as an important regulator of presynaptic architecture and function. Furthermore, our findings strongly indicate that the tethering machinery plays a critical role in synaptic vesicle exocytosis and suggest a structural mechanism for RIM1α priming action.

Results

Synaptic vesicle distribution and AZ morphology in RIM1α KO synapses

General morphology of vitrified frozen-hydrated cerebrocortical synaptosomes from RIM1α KO and WT littermate mice (Fig. 1, A, D, and F) was comparable to that previously observed in rat synaptosomes and rat organotypic slices (Fernández-Busnadiego et al., 2010). Synaptosome diameter and thickness ranged from 0.5 to 1 µm and 300 to 500 nm, respectively. Membranes appeared smooth and continuous, and there were no signs of aggregation of cytoplasmic components, as expected for vitrified specimens. Terminals typically contained

Bars, 100 nm. B, E, and G show corresponding 3D renderings of all vesicles within 250 nm from the AZ (left) and of the AZ and proximal vesicles seen from the cytoplasmic side (right). AZ (gray), synaptic vesicles (yellow), tethers (blue), connectors (red) are shown. For scale reference, mean vesicle diameter was 40.1 ± 5.4 nm (mean ± SD; no scale bars are shown because the image is rendered with 3D perspective). RIM1α KO-altered synapses showed reduced number of proximal vesicles and vesicle tethering to the AZ. (C) Magnified views of connectors (black arrowheads) and tethers (white arrowheads). Bars, 50 nm. Tomographic slices are 5.4 nm thick. Video 1, Video 2, and Video 3 are related.

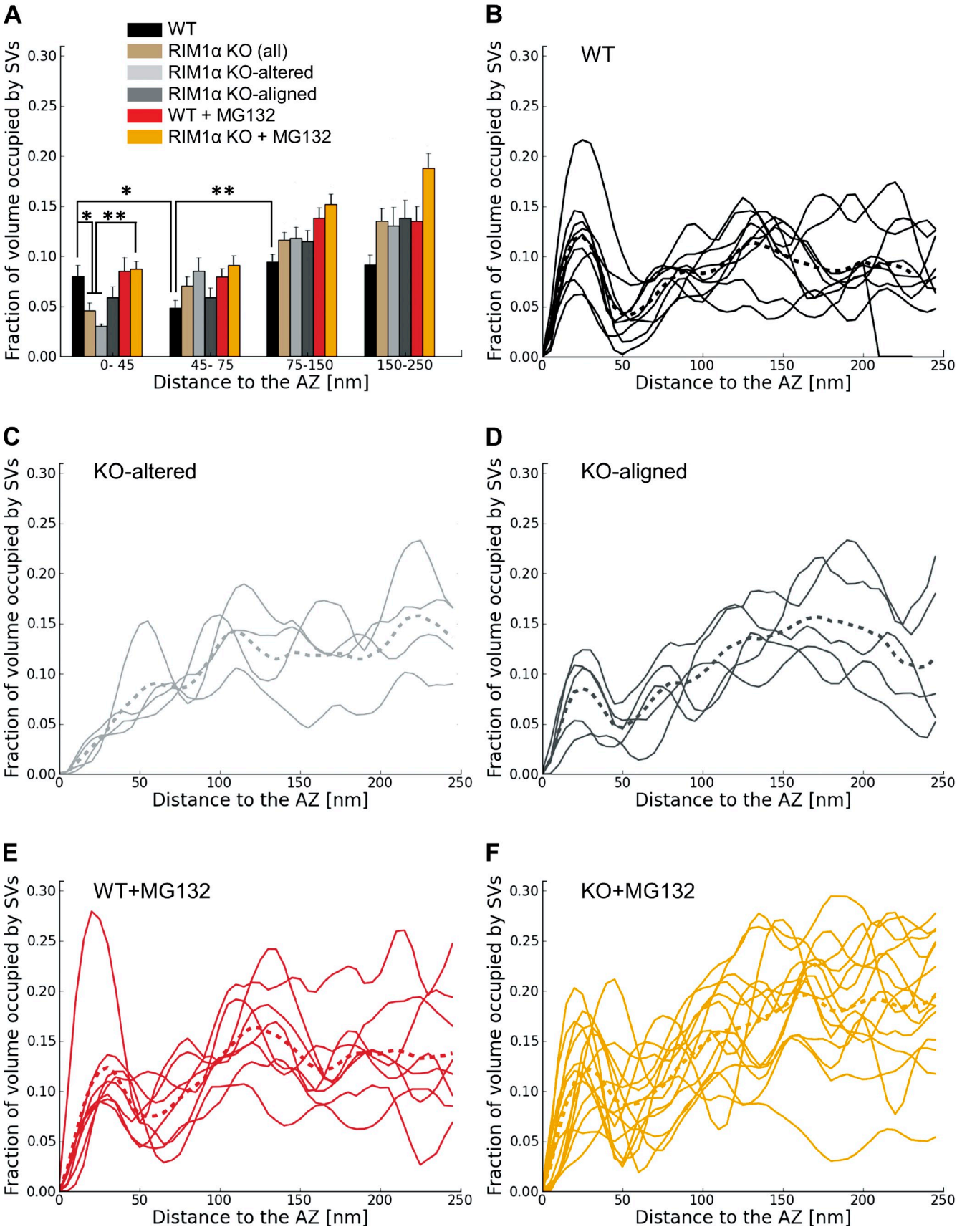

Figure 2. **Synaptic vesicle concentration.** For vesicles within 250 nm from the AZ, shown as the fraction of cytoplasmic volume occupied by vesicles, according to their distance to the AZ. (A) Mean vesicle concentration versus distance to the AZ. Error bars show SEMs. Proximal vesicle concentration was significantly reduced in RIM1α KO. (B–F) Individual vesicle concentration profiles for all synapses in WT, KO-altered, KO-aligned, WT + MG132, and

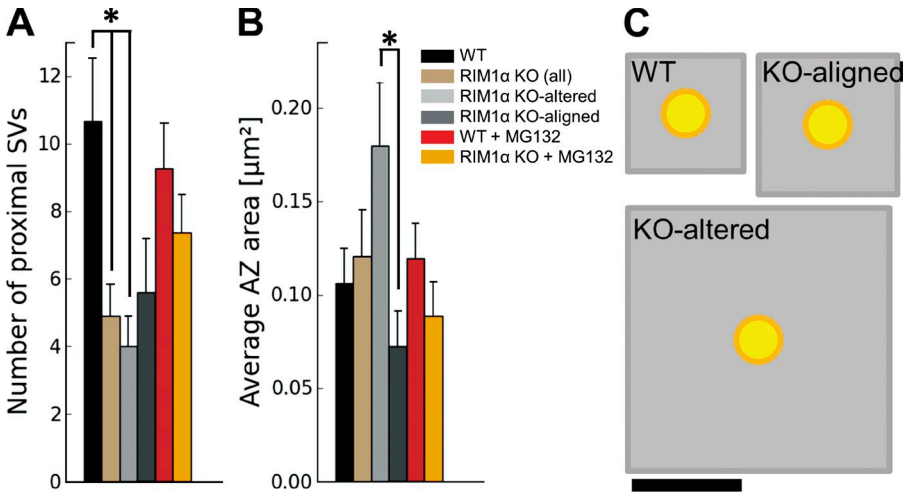

Figure 3. **AZ organization.** (A) Number of proximal synaptic vesicles (SV; within 45 nm from the AZ) per synapse, which was significantly reduced in RIM1α KO synapses. (B) Average AZ area. A and B show mean values and SEMs (error bars). Confidence value: *, $P < 0.05$. The numbers of animals, synapses, and vesicles analyzed for each category are shown in Table S1. (C) Quantitative representation of AZ area (gray) per proximal vesicle (yellow), calculated as the total AZ area (B) divided by the number of proximal vesicles (A). Bar, 100 nm.

100–500 synaptic vesicles embedded in a dense presynaptic cytomatrix predominantly formed by vesicle connectors and tethers (Fig. 1, A, C, and F).

We first compared synaptic vesicle distribution in RIM1α KO and WT synapses by measuring the fraction of cytoplasmic volume occupied by vesicles (vesicle concentration). All WT synapses (Fig. 1, A and B; and Video 1) showed a characteristic vesicle concentration profile, with a maximum close to the AZ (0–45 nm) and a minimum 45–75 nm away from the AZ ($n = 9$; Fig. 2 B). This concentration profile was remarkably similar to our previous observations in rat cortical synapses and was used as reference to divide the presynaptic terminal into four zones, reflecting the maxima and minima observed in the individual profiles: proximal (0–45 nm to the AZ, where the maximum of vesicle concentration was located), intermediate (45–75 nm, containing the concentration minimum), and two distal zones of similar thickness further away from the AZ (first: 75–150 nm; and second: 150–250 nm; Fernández-Busnadiego et al., 2010). We refer to vesicles within the proximal zone (0–45 nm to the AZ) as proximal vesicles. Taking all WT synapses together, vesicle concentration was significantly lower in the intermediate than in the proximal and distal zones ($P < 0.05$ and $P < 0.01$ by *t* test, respectively; Fig. 2 A).

In contrast to WT synapses, RIM1α KO terminals displayed considerable heterogeneity. We identified two subpopulations of synapses according to the existence of vesicle concentration maxima within the proximal zone. Five out of nine KO synapses (termed KO aligned; Fig. 1, F and G; and Video 3) showed vesicle concentration maxima in the proximal zone and a vesicle concentration profile roughly aligned with that of WT terminals (Fig. 2 D). The other KO synapses (four out of nine, termed KO altered; Fig. 1, D and E; and Video 2) showed a markedly disturbed profile (Fig. 2 C), with 60% lower vesicle concentration in the proximal zone compared with WT ($P < 0.05$ by *t* test; Fig. 2 A). Both types of synapses were found in all KO mice analyzed. Taking all KO synapses together, vesicle concentration was reduced by 40% in the proximal zone ($n = 9$, $P < 0.05$ by *t* test; Fig. 2 A). On average, this translated into a reduction from 10.7 ± 1.8 (WT) to 4.9 ± 1.0 (all KO together) and 4.0 ± 0.9 (KO altered only) proximal vesicles per AZ (mean ± SEM; $P < 0.05$ by *t* test in both cases; Fig. 3 A).

The differences between KO subgroups were likely not based on their inhibitory/excitatory character because most synapses had a prominent postsynaptic density (WT: seven out of nine; KO aligned: four out of five; KO altered: four out of four; Fig. 1, A, D, and F), and no major differences in synaptic transmission were measured between inhibitory and excitatory synapses in RIM1α KO mice (Kaeser et al., 2008). On the other hand, immunostaining experiments revealed that the fraction of presynaptic terminals (marked by VAMP2/synaptobrevin2 staining) positive for MUNC13 was reduced in RIM1α KO synaptosomes ($P < 0.001$ by *t* test; Fig. S1, C and D), whereas the fraction of RIM1-positive terminals increased ($P < 0.001$ by *t* test; Fig. S1, A and D), likely because of the up-regulation of RIM1β (Kaeser et al., 2008). Other AZ proteins, such as RIM2 or ELKS, showed no significant differences (Fig. S1, B and D). Therefore, deletion of RIM1α led to significant changes in some of the remaining AZ components in a subset of synapses, likely contributing to the structural differences between KO subgroups.

In agreement with previous work (Schoch et al., 2002), mean AZ area in KO synapses was comparable to that of WT (Fig. 3 B). However, the AZ was significantly larger in KO-altered than in KO-aligned terminals ($P < 0.05$ by *t* test; Fig. 3 B). Compared with WT, the mean AZ area per proximal vesicle showed a threefold increase for all KO terminals (NS) and fivefold increase for KO-altered synapses alone ($P < 0.01$ by *t* test; Fig. 3 C). As previously shown in neuronal cultures (Schikorski and Stevens, 1997), the number of proximal vesicles was well correlated with AZ area in WT (Pearson correlation, $P < 0.01$

KO + MG132 categories, respectively. Thicker dotted profiles represent means. Confidence values: *, $P < 0.05$; **, $P < 0.01$. Whereas all WT synapses showed a characteristic profile, RIM1α KO synapses were classified in two subpopulations (KO altered and KO aligned) according to the existence of vesicle concentration maxima within the proximal zone. In contrast, most MG132-treated RIM1α KO synapses showed a concentration profile comparable to WT. The numbers of animals, synapses, and vesicles analyzed for each category are shown in Table S1. SV, synaptic vesicle.

Table 1. **Correlation between AZ area and number of proximal vesicles**

Condition	Pearson correlation coefficient	P-value
WT	0.82	<0.01
KO	0.07	>0.05
WT + MG132	0.80	<0.05
KO + MG132	0.76	<0.01

Statistical significance (p-values) was determined by *t* test. The numbers of animals, synapses, and vesicles analyzed for each category are shown in Table S1.

by *t* test; Table 1), whereas this correlation was completely lost in KO terminals (Pearson correlation, $P > 0.05$ by *t* test; Table 1). Proximal vesicles appeared randomly distributed at the AZ and did not cluster at specific AZ locations for all animals (Fig. 1, B, E, and G). Collectively, these results show that deletion of RIM1α caused severe alterations in vesicle distribution and AZ morphology.

Presynaptic cytomatrix defects in the absence of RIM1α

Similarly to our observations in rat synaptosomes and organotypic slices (Fernández-Busnadiego et al., 2010), proximal synaptic vesicles in synaptosomes from WT and KO mice were in most cases linked to the AZ by filamentous tethers (Fig. 1, A, C, and F) and made direct membrane to membrane contact with the AZ only during exo/endocytosis. On average, there were 6.4 ± 1.1 vesicles tethered to the AZ in WT synapses (mean ± SEM; Fig. 4 A), representing 60% of the proximal vesicles (Fig. 4 B). This number was reduced to 1.7 ± 0.9 in KO-altered terminals (mean ± SEM; $P < 0.05$ by *t* test; Fig. 4 A). The number of tethers per unit of AZ surface was also dramatically reduced in KO-altered synapses ($P < 0.01$ by *t* test; Fig. 4 D). In KO-aligned terminals, the number of tethered vesicles per synapse was slightly reduced (NS), likely caused by the reduction in the total number of proximal vesicles (Fig. 2, A and D; and Fig. 3 A).

We previously proposed that vesicles with multiple short tethers are structurally primed and belong to the RRP, as these vesicles were depleted by hypertonic sucrose (Fernández-Busnadiego et al., 2010). Interestingly, the population of vesicles with more than two tethers was completely absent in KO-altered synapses, whereas in KO aligned, these vesicles were similarly abundant as in WT (Fig. 4 C). In WT terminals, the distance between vesicles and the AZ was inversely correlated with the number of tethers per vesicle (Pearson correlation, $P < 0.001$ by *t* test; Table 2), whereas this correlation was lost in RIM1α KO (Pearson correlation, $P > 0.05$ by *t* test; Table 2). In fact, tether length increased significantly in KO synapses ($P < 0.01$ by Kruskal-Wallis [K-W] test; Fig. 4 E and Fig. S2), and the fraction of short tethers was significantly reduced ($P < 0.01$ by χ^2 test; Fig. 4 F). This difference was more pronounced in KO-altered synapses, in which tethers were ∼70% longer than in WT ($P < 0.05$ by K-W test; Fig. 4 E and Fig. S2). Therefore, our data showed significant tethering defects in KO synapses, which were especially prominent in the KO-altered subgroup. Together with the reduction of proximal vesicle concentration, these tethering defects suggest significant release deficits and RRP reduction in RIM1α KO synapses—and in particular in KO-altered synapses—in agreement with electrophysiological data (Schoch et al., 2002; Calakos et al., 2004).

Connectors linked ∼60% of vesicles to each other in WT terminals. Connectivity increased very significantly in all KO synapses, both measured as the fraction of connected vesicles ($P < 0.001$ by *t* test; Fig. 5 A) and the mean number of connectors per vesicle ($P < 0.001$ by K-W test; Fig. 5 C). In the proximal zone, connectivity increased in all KO synapses, more prominently in the KO-aligned case ($P < 0.01$ by *t* test in both cases; Fig. 5 B). Because, in KO-aligned terminals, most proximal vesicles were tethered ($P < 0.01$ by χ^2 test; Fig. 4 B), almost 80% of proximal vesicles in these synapses were both tethered and connected ($P < 0.001$by χ^2 test; Fig. 5 D and Fig. S2). Synaptic vesicle diameter increased in all KO synapses ($P < 0.001$ by *t* test; Fig. S3, A and B), leading to a mean increase in vesicle volume of 26% in KO terminals. Thus, the lack of the AZ protein RIM1α perturbed cytomatrix architecture and synaptic vesicle size not only at the AZ but also in more distal areas.

The UPS in RIM1α KO presynaptic terminals

Proteasomes are active in mouse brain synaptosomes (Upadhya et al., 2006; Tai et al., 2010). To investigate the roles of the UPS in presynaptic architecture and its possible structural interactions with RIM1α, we analyzed WT and RIM1α KO synaptosomes treated with the reversible proteasome inhibitor MG132 (10 µM; 30 min at 37°C), the most widely used proteasome inhibitor in synaptic studies (Kalla et al., 2006; Yao et al., 2007; Jiang et al., 2010; Rinetti and Schweizer, 2010; Tada et al., 2010; Lazarevic et al., 2011). Terminals from both WT and RIM1α KO brains showed similar proteasomal activity, which was suppressed to a large extent by incubation with MG132 (Fig. S4).

Western blot analysis confirmed that RIM1α was not detectable in KO terminals (Fig. 6). As previously reported (Schoch et al., 2002; Kaeser et al., 2008), MUNC13 levels were markedly reduced in RIM1α KO, whereas other presynaptic proteins, such as RIM2, ELKS, Liprin2, Liprin3, Rab3, synaptotagmin1, or the SNARE proteins syntaxin1, SNAP25, and VAMP2, remained unchanged, and RIM1β was up-regulated. Incubation with MG132 induced an accumulation of ubiquitinated proteins that was more prominent for KO mice (n = 3–4 WT and KO pairs of littermate mice for ELKS, Liprin2, Liprin3, Rab3, synaptotagmin1, syntaxin1, SNAP25, VAMP2, and ubiquitin). In agreement with previous studies (Yao et al., 2007; Lazarevic et al., 2011), proteasome inhibition caused a moderate increase in RIM1α and MUNC13 levels in WT synapses. The levels of RIM1β and MUNC13 increased in MG132-treated KO terminals (n = 7 WT and KO pairs of littermate mice), in which a less pronounced increase in RIM2 levels upon MG132 treatment was also observed (n = 6 WT and KO pairs of littermate mice). Therefore, the reduction in the levels of the critical priming factors RIM and MUNC13 observed in RIM1α KO was partially alleviated by proteasome inhibition.

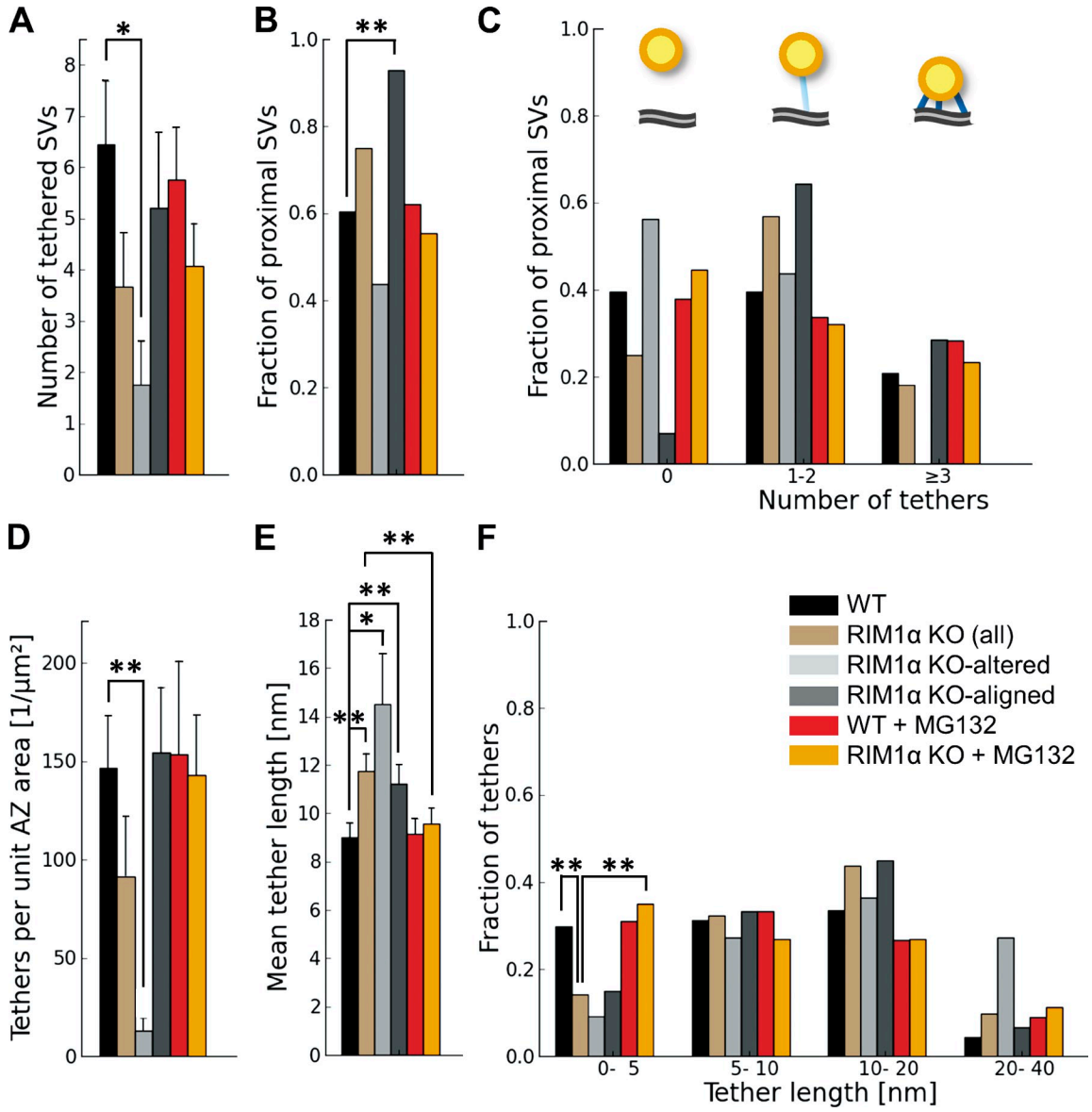

Figure 4. **Synaptic vesicle tethers to the AZ.** For proximal vesicles (within 45 nm from the AZ, as virtually no vesicles were tethered in more distal areas). (A) Number of tethered vesicles per synapse, which was strongly reduced in RIM1α KO-altered synapses. (B) Fraction of proximal vesicles tethered to the AZ. (C) Histogram of number of tethers per proximal vesicle. Note that no vesicles with more than two tethers were found in KO-altered synapses. (top) The cartoon represents the bins of the histogram: nontethered vesicles (left), vesicles with one to two tethers (middle), and vesicles with multiple tethers (right). AZ (gray), proximal vesicles (yellow), and tethers (blue) are shown. (D) Number of tethers per AZ unit area. (E) Tether length. (F) Histogram of tether lengths. Short tether formation was impaired in RIM1α KO synapses. A, D, and E show mean values and SEMs (error bars). B, C, and F show number of occurrences (consequently no error bars are displayed). Confidence values: *, $P < 0.05$; **, $P < 0.01$. The numbers of animals, synapses, vesicles, and tethers analyzed for each category are shown in Table S1. SV, synaptic vesicle.

Proteasome inhibition reverses the structural and functional defects at RIM1α KO AZs and increases vesicle diameter and connectivity

General morphology of synapses treated with the proteasome inhibitor MG132 was comparable to control (Fig. 7). In WT, vesicle distribution and tethering were largely unaffected by MG132 (Fig. 2, A and E; and Fig. 4). Surprisingly, in 12 out of 14 KO synapses treated with MG132, vesicle distribution was comparable to WT (Fig. 2 F). Furthermore, the correlation between AZ area and the number of proximal vesicles in MG132-treated KO terminals was restored to WT levels (Pearson correlation,

Table 2. **Correlation between number of tethers per vesicle and vesicle distance to the AZ**

Condition	Pearson correlation coefficient	P-value
WT	−0.44	<0.001
KO	−0.28	>0.05
WT + MG132	−0.54	<0.001
KO + MG132	−0.48	<0.001

Statistical significance (p-values) was determined by *t* test. The numbers of animals, synapses, vesicles, and tethers analyzed for each category are shown in Table S1.

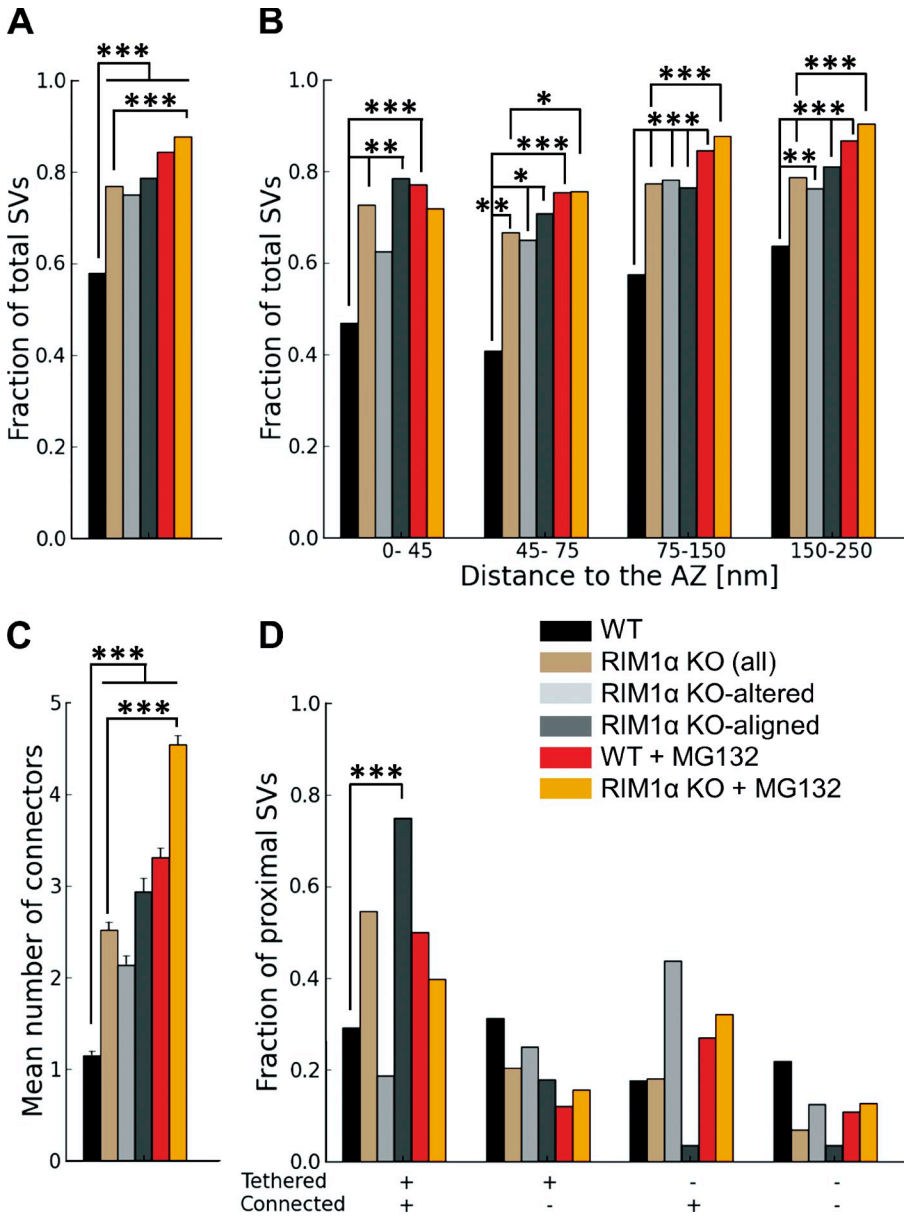

Figure 5. **Synaptic vesicle connectors for vesicles within 250 nm from the AZ.** Connectivity increased both in WT and RIM1α KO under MG132 treatment. (A) Fraction of connected vesicles. (B) Fraction of connected vesicles versus distance to the AZ. (C) Mean number of connectors per vesicle. (D) Fraction of vesicles as a function of tethering and connectivity. C shows mean values and SEMs (error bars). A, B, and D show number of occurrences (consequently no error bars are displayed). Confidence values: *, $P < 0.05$; **, $P < 0.01$; ***, $P < 0.001$. The numbers of animals, synapses, vesicles, and connectors analyzed for each category are shown in Table S1. SV, synaptic vesicle.

$P < 0.01$ by *t* test; Table 1), and vesicle concentration increased significantly at the AZ ($P < 0.01$ by *t* test; Fig. 2 A), reaching WT levels. Thus, proteasome inhibition reversed to a large extent the vesicle distribution defect caused by lack of RIM1α.

MG132 treatment also caused a significant reduction in mean tether length in KO terminals ($P < 0.01$ by K-W test; Fig. 4 E) and increased the fraction of short tethers ($P < 0.01$ by *t* test; Fig. 4 F), making both of these comparable to WT. Furthermore, the inverse correlation between the number of tethers per vesicle and the vesicle distance to the AZ was restored in MG132-treated KO terminals (Pearson correlation, $P < 0.001$ by *t* test; Table 2). In addition, RIM1α KO terminals treated with MG132 were indistinguishable from WT in terms of number of tethered vesicles, tethered vesicle fraction, tethers per vesicle, and tethers per unit AZ surface (Fig. 4, A–D). Therefore, the tethering deficit observed in untreated KO terminals was fully rescued by MG132.

We next asked whether the structural recovery observed in RIM1α KO terminals upon MG132 treatment was paralleled by a rescue of presynaptic function. To that end, we examined paired-pulse facilitation (PPF) in hippocampal slices by measuring extracellular field potentials (field excitatory postsynaptic potentials [fEPSPs]) in the CA1 region. PPF is the enhancement of neurotransmitter release in response to two closely spaced stimuli and is inversely correlated with synaptic vesicle release probability (Thomson, 2000). In agreement with previous work (Schoch et al., 2002), RIM1α KO synapses showed a significant increase in PPF ($P < 0.01$ by *t* test; Fig. 8), indicating reduced release probability. Strikingly, this defect was completely reversed by MG132 ($P < 0.01$ by *t* test; Fig. 8), as MG132-treated RIM1α KO synapses showed comparable PPF to WT synapses. Thus, the reduction in release probability of RIM1α KO synapses was rescued by proteasome inhibition. MG132 did not have a significant effect on PPF of WT terminals, consistently with our structural

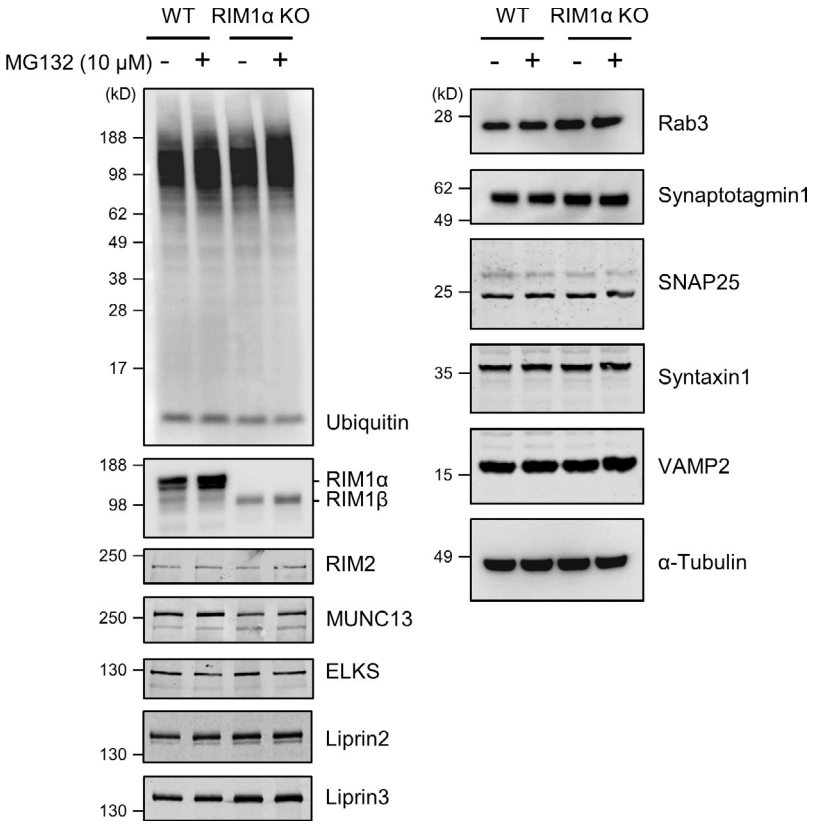

Figure 6. **Western blot analysis for ubiquitin and various presynaptic proteins.** The double band detected for RIM1α corresponds to splice variants (see, e.g., Fig. 1 of Kaeser et al., 2008). MG132 induced an increase in the levels of RIM1α (WT), RIM1β (KO), and MUNC13 (WT and KO) and a smaller increase in RIM2 (KO) but not in other presynaptic proteins. Sample sizes (pairs of WT and KO littermates) are as follows: seven (RIM1 and MUNC13), six (RIM2), and three to four (ELKS, Liprin2, Liprin3, Rab3, synaptotagmin1, syntaxin1, SNAP25, VAMP2, and ubiquitin).

results showing no alterations in tethering or proximal vesicle concentration (Fig. 2, A and E; and Fig. 4). Altogether, these data establish a direct correlation between those structural features and presynaptic function.

Proteasome inhibition induced as well a significant increase in the fraction of connected vesicles ($P < 0.001$ by *t* test; Fig. 5 A) and the number of connectors per vesicle ($P < 0.001$ by K-W test; Fig. 5 C) in both WT and RIM1α KO, indicating that synaptic vesicle connectors are regulated by the UPS. Vesicle diameter increased in WT and KO synapses treated with MG132 ($P < 0.001$ by *t* test in both cases; Fig. S3, A and B), leading to a 37 and 17% increase in vesicle volume, respectively. These data strongly indicate that the UPS regulates key presynaptic parameters, such as vesicle size, vesicle distribution, and connector and tether formation.

Discussion

Even though RIM1α-deficient mice exhibit multiple presynaptic defects resulting in impaired memory and learning, no underlying ultrastructural alterations were found in chemically fixed EM preparations. Here, we have analyzed vitrified frozen-hydrated presynaptic terminals by cryo-ET, revealing that RIM1α KO synapses do show prominent structural abnormalities in terms of vesicle distribution and presynaptic cytomatrix organization. Proteasome inhibition not only reversed the defects in vesicle distribution and tethering of KO synapses but also rescued their functional deficits as assessed by electrophysiological recordings, further demonstrating the critical role of the tethering machinery in synaptic vesicle exocytosis.

The release deficit of RIM1α KO synapses is caused by structural defects at the AZ that can be rescued by proteasome inhibition

RIM1α KO synapses showed a 40% reduction of proximal vesicles at the AZ with respect to WT (Fig. 2 A and Fig. 3 A), accompanied by defects in vesicle tethering to the AZ. We have previously proposed that the number and length of tethers determine vesicle availability for release, so that vesicles with multiple short tethers are structurally primed for fusion (Fernández-Busnadiego et al., 2010). This model is consistent with the in vitro observations that the fusion machinery precisely regulates intermembrane distance and thereby vesicle fusogenicity (Li et al., 2007; van den Bogaart et al., 2011). Accordingly, here, we show that in WT synapses the distance of proximal vesicles to the AZ was inversely correlated with the number of tethers (Table 2). This correlation was lost in RIM1α KO synapses, where defects in short tether formation (Fig. 4 F) significantly increased mean tether length (Fig. 4 E). Therefore, it is likely that the strong reduction of proximal vesicles together with defects in maturation of the tethering machinery account for the reduction in release probability and RRP size in RIM1α KO synapses (Fig. 8; Schoch et al., 2002; Calakos et al., 2004).

In contrast to WT, where all synapses analyzed were highly homogeneous in terms of vesicle distribution and organization of the presynaptic cytomatrix, synapses from RIM1α KO mice could be clearly classified in two separate categories. The alterations in vesicle distribution and AZ tethering were relatively mild in a subgroup of synapses (KO aligned; Fig. 2, A and D; and Fig. 4). In the other subgroup (KO altered), the number of

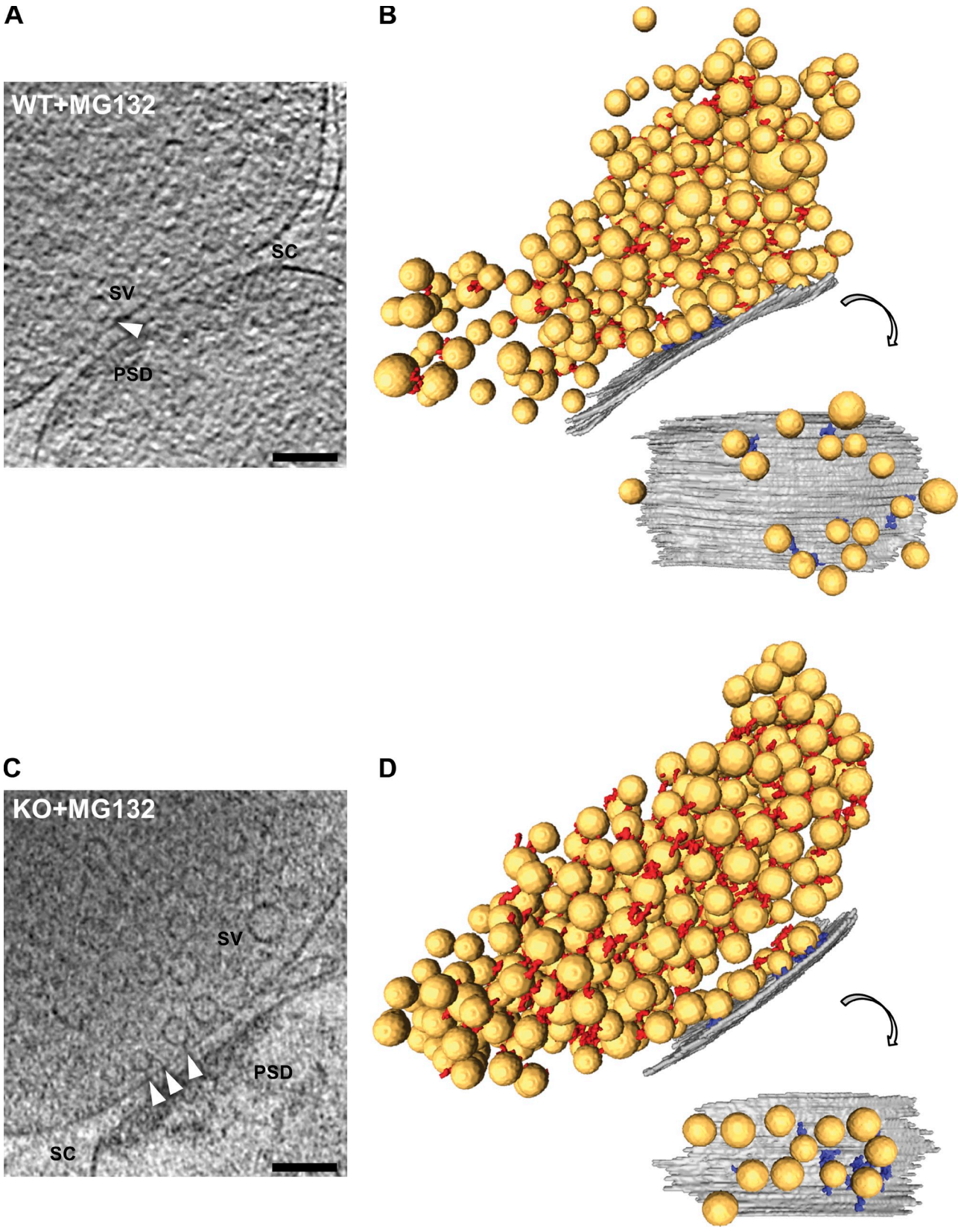

Figure 7. **Morphology of MG132-treated WT and RIM1α KO synapses by cryo-ET.** (A and C) Tomographic slices of MG132-treated WT (A) and RIM1α KO (C) synapses. PSD, postsynaptic density; SC, synaptic cleft; SV, synaptic vesicle; white arrowheads, tethers. Tomographic slices are 5.4 nm thick. Bars, 100 nm. B and D show corresponding 3D renderings of all vesicles analyzed (left) and of the AZ and proximal vesicles seen from the cytoplasmic side (right). AZ (gray), synaptic vesicles (yellow), tethers (blue), and connectors (red) are shown. For scale reference, mean vesicle diameter was 40.1 ± 5.4 nm (mean ± SD; no scale bars are shown because the image is rendered with 3D perspective). MG132-treated WT and RIM1α KO synapses were comparable in terms of proximal vesicle concentration and vesicle tethering to the AZ.

proximal vesicles (Fig. 2, A and C; and Fig. 3 A) and the number of tethers per unit AZ surface were drastically reduced (Fig. 4 D). Additionally, vesicles completely failed to form multiple tethers to the AZ (Fig. 4 C), and the formation of shorter filaments was strongly impaired in KO-altered synapses (Fig. 4 F and Fig. S2). Therefore, our data show that the tethering and synaptic vesicle organization defects were especially prominent in KO-altered terminals, arguing that release is likely strongly reduced in these synapses.

Vesicle distribution and tethering to the AZ in WT synapses were largely unaffected by the proteasome inhibitor MG132 (Fig. 2 A, E and Fig. 4), in agreement with previous work reporting no effect of MG132 on the RRP (Jiang et al., 2010). However, mutant synapses treated with MG132 showed a sharp increase in vesicle concentration at the AZ with respect to untreated KO synapses (Fig. 2, A and F). Average tether length was reduced (Fig. 4 E) because of enhanced formation of short tethers (Fig. 4 F), and the correlation between AZ vesicle distance and number of tethers per vesicle was restored to WT levels (Table 2), making MG132-treated RIM1α KO AZs indistinguishable from WT ones. Therefore, proteasomal inhibition rescued the structural phenotype of the mutant synapses.

Importantly, electrophysiological recordings showed that although MG132 had no significant effect on PPF in WT terminals, this compound completely abolished the reduction in release probability caused by RIM1α deletion (Fig. 8). Thus, presynaptic terminals indistinguishable in terms of vesicle tethering to the AZ (WT, MG132-treated WT, and MG132-treated RIM1α KO; Fig. S2) presented nearly identical release probability, whereas synapses with tethering alterations were also functionally compromised (RIM1α KO). These data strongly support the hypothesis that the release deficit of RIM1α KO synapses is caused by a reduced number of proximal vesicles and defects in tether formation. More generally, our results show a direct correspondence between structural and functional aspects of neurotransmitter release and reveal the critical role of the tethering machinery in synaptic vesicle exocytosis. Our data further suggest that the modulation of vesicle tethering may be one of the mechanisms by which the UPS regulates presynaptic homeostatic plasticity in a terminal-specific manner (Jiang et al., 2010; Lazarevic et al., 2011).

Molecular mechanisms of synaptic vesicle tether formation

The analysis of an extensive list of proteins showed that only MUNC13 is down-regulated in RIM1α KO brains (Fig. 6; Schoch et al., 2002, 2006; Kaeser et al., 2008). In fact, the synaptic recruitment and priming action of MUNC13 occur downstream of RIM (Jiang et al., 2010; Deng et al., 2011). Even though other proteins not yet analyzed may also be involved, these data argue that the tethering defects in RIM1α KO were most likely a result of the lack of RIM1α and/or the reduction in MUNC13 levels, indicating that RIM1α and/or MUNC13 play important roles in tether formation.

Additional proteins beyond RIM1α must be involved in tether formation because some tethers persisted in RIM1α KO synapses. RIM1β is the only synaptic protein found to be up-regulated in RIM1α KO (Fig. 6 and Fig. S1; this study; Kaeser et al., 2008), and its overexpression rescues the priming defect of RIM1/2 KO almost completely (Deng et al., 2011). Also, RIM2α and RIM1β are the only other RIM isoforms containing the zinc finger domain that interacts with MUNC13 (Mittelstaedt et al., 2010). Therefore, it is plausible that RIM1β partially compensates for the deletion of RIM1α, whereas the involvement of RIM2α cannot be excluded.

Previous studies identified RIM (Yao et al., 2007; Jiang et al., 2010; Lazarevic et al., 2011) and MUNC13 (Aravamudan and Broadie, 2003; Speese et al., 2003; Kalla et al., 2006; Rinetti and Schweizer, 2010; Tada et al., 2010; Lazarevic et al., 2011) as targets of the UPS. Incubation of WT and RIM1α KO synaptosomes with MG132 strongly reduced proteasome activity in synaptosomes (Fig. S4), leading to a moderate increase in RIM1β, RIM2, and MUNC13 levels in KO synapses (Fig. 6). We hypothesize that such increase allowed the formation of a sufficient number of RIM–MUNC13 priming complexes to rescue the structural and functional phenotype of RIM1α KO synapses because, locally at the AZ, only a small number of molecules (tethers) differentiates WT from KO synapses. In such a scenario, the ability of cryo-ET to image individual protein complexes appears to correlate better with electrophysiological measurements that assess synaptic function directly (Fig. 8) than techniques analyzing total protein levels such as Western blotting.

Higher levels of compensatory proteins in KO-aligned than in KO-altered synapses may explain the stronger tethering defects observed in the latter subgroup. In fact, several lines of evidence point to heterogeneous synaptic levels of RIMs and MUNC13 in RIM1α KO brains: (a) RIMs have overlapping but distinct expression patterns (Schoch et al., 2006; Kaeser et al., 2008), and thus, synapses with higher RIM1α expression levels and/or lower levels of other RIMs will be more profoundly affected by RIM1α deletion, (b) the fraction of presynaptic terminals positive for RIM1 and MUNC13 was altered in RIM1α KO synaptosomes (Fig. S1), likely because not only the levels but also the distributions of RIM1β and MUNC13 are altered in RIM1α KO (Andrews-Zwilling et al., 2006; Kaeser et al., 2008), and (c) the levels of compensatory RIMs at a particular RIM1α KO synapse may be homeostatically influenced by its activity (Jiang et al., 2010; Lazarevic et al., 2011).

Our data are consistent with previous studies implicating RIM and MUNC13 in synaptic vesicle tethering and docking. RIM but not MUNC13 is likely involved in the initial tethering-mediated association of vesicles to the AZ (Fig. 9) because the number of vesicles within 45 nm from the AZ was reduced in the RIM1α KO (Fig. 2 A and Fig. 3 A; this study) and even more strongly in the KO of all RIM 1/2 isoforms (Han et al., 2011; Kaeser et al., 2011) but not in MUNC13-1/2 double KO (Siksou et al., 2009). The formation of multiple tethers of decreasing length is structurally correlated with vesicle priming and likely depends on SNAREs (Fernández-Busnadiego et al., 2010). Our results suggest that RIM1α and possibly other RIMs are involved in the transition between few and multiple tethers, perhaps by forming a complex with MUNC13 (Fig. 9). In turn MUNC13, which was proposed to act as a tether based on the structural similarity of its C-terminal module with tethering factors,

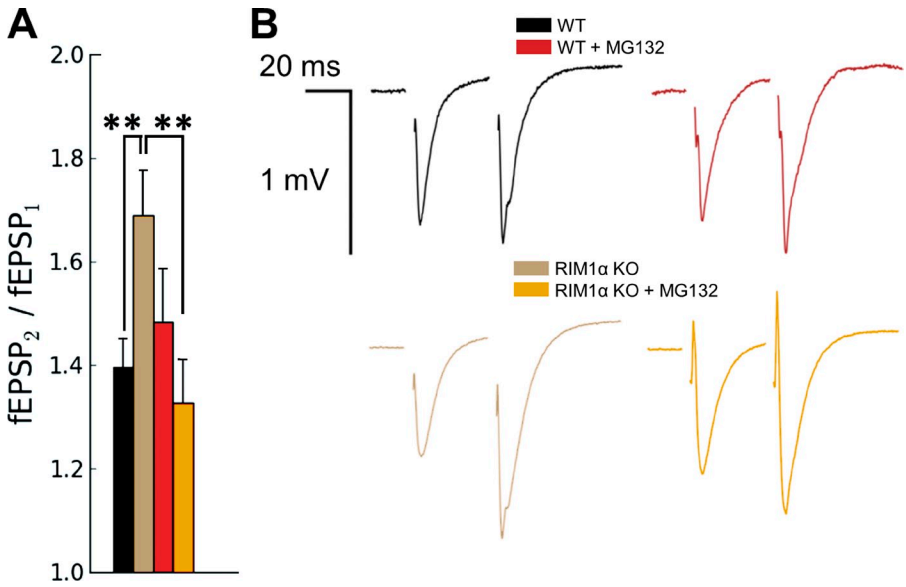

Figure 8. **Excitatory synaptic responses to paired-pulse stimulation in WT and RIM1α KO mice in the absence and presence of MG132.** (A) PPF ($fEPSP_2/fEPSP_1$) recorded in stratum radiatum of CA1. The graph shows mean values and SEMs (error bars). Confidence values: **, $P < 0.01$. Compared with WT mice, RIM1α KO mice showed an increase in PPF that was reversed by MG132 treatment. (B) Representative traces. Sample sizes are as follows (slices/animals): WT, 14/4; WT + MG132, 16/4; RIM1α KO, 14/4; and RIM1α KO + MG132, 13/4.

may facilitate SNARE complex assembly (Li et al., 2011; Ma et al., 2011, 2013). However, we cannot exclude that the defects in short tether formation in the RIM1α KO could be exclusively caused by the reduction in MUNC13 levels in these mice. Our data are in good agreement with the reduction of docked vesicles likely underlying the priming defect of MUNC13-1/2 double KO synapses (Siksou et al., 2009) because the vesicles that we identify as structurally primed probably correspond to docked vesicles in fast-frozen, dehydrated, and heavy metal–stained samples. In that preparation, the membrane of docked vesicles did not touch the AZ directly but via short tethers that were obscured by membrane staining (Siksou et al., 2011). Thus, in all fast-frozen preparations, both in synaptosomes and hippocampal slices, direct membrane to membrane contact between vesicles and the AZ is only observed during exo/endocytosis and not at the docking step. Even though we cannot clarify whether RIM or MUNC13 are constitutive elements of the tethers or act upstream of tether formation, our results suggest that RIM is involved in the initial AZ tethering, whereas the structural correlate of vesicle priming is the formation of multiple tethers of decreasing length, which likely depends on RIM and MUNC13 (Fig. 9).

On the other hand, additional proteins are likely involved in AZ tethering. Bruchpilot is required for tethering in the *Drosophila melanogaster* neuromuscular junction (Hallermann et al., 2010b), but its mammalian homologue ELKS has a different domain structure, and its synaptic function is unclear (Südhof, 2012). Also, beyond its well-characterized roles as Ca^{2+} sensor, synaptotagmin1 may as well act as vesicle docking agent and distance regulator (de Wit et al., 2009; van den Bogaart et al., 2011). Even though some of these proteins are also regulated by the UPS (Lazarevic et al., 2011), our results showed no significant changes in ELKS, liprins, or synaptotagmin1 upon proteasome inhibition (Fig. 6 and Fig. S1). Lastly, in Piccolo/Bassoon double mutants, the number of proximal vesicles was reduced, but synaptic transmission was unaltered except under high frequency stimulation (Hallermann et al., 2010a; Mukherjee et al., 2010), arguing against a major contribution of these proteins to the structural and functional rescue of the RIM1α KO phenotype by proteasome inhibition.

AZ architecture and the UPS modulate vesicle size and connectivity

Connectors play a fundamental role in vesicle clustering (Fernández-Busnadiego et al., 2010). Connectivity was higher in

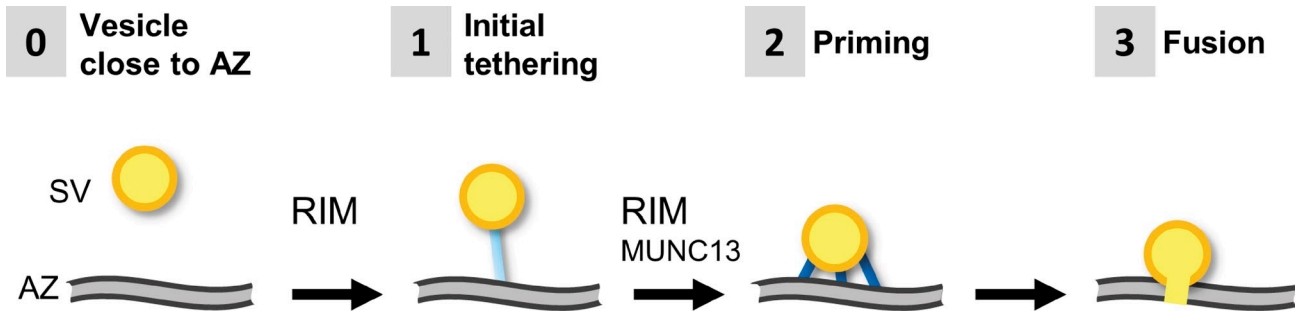

Figure 9. **Model for RIM-mediated synaptic vesicle priming.** In WT terminals, vesicles (synaptic vesicle [SV]) that are close to the AZ (0) are first linked to the AZ (1) by one or few tethers (blue rods) in a RIM-dependent process. Likely by the action of RIM and MUNC13, vesicles progressively acquire additional shorter tethers, thereby reducing the distance between vesicle and AZ. Vesicles with multiple tethers are primed for release (2), and primed vesicles can fuse upon Ca^{2+} influx (3).

all RIM1α KO synapses, leading to a more tightly interlinked vesicle cluster (Fig. 5). Rather than a direct effect of RIM1α, exclusively localized at the AZ (Tao-Cheng, 2006; Dani et al., 2010), this suggests that defects in AZ architecture propagate into cytomatrix alterations through the whole terminal.

Proteasome inhibition caused a very significant increase in vesicle connectivity in WT and KO synapses (Fig. 5), indicating that connectivity and consequently vesicle clustering are regulated by the UPS. In the simplest scenario, connectors might be degraded by the proteasome, and thus, their numbers increase upon proteasome inhibition. Interestingly, molecular candidates to form connectors, such as synapsin (Hirokawa et al., 1989), have been reported to be targets of proteasomal degradation (Fioravante et al., 2008; Lazarevic et al., 2011). Nevertheless, the exact roles of synapsin remain unclear, as some connectors persisted in synapsin triple KO mice (Siksou et al., 2007).

Even though PPF and release probability are inversely correlated, the mechanistic link between them is not well understood. Our data show that a reduced number of proximal vesicles and tethering defects underlie the reduction in release probability in RIM1α KO synapses and suggest that the corresponding increase in PPF (Fig. 8; Schoch et al., 2002; Calakos et al., 2004) could be caused by a cross talk between tethering and connectivity, which could also shed light on the fate of connectors upon vesicle release. Namely, in RIM1α KO, in which one subgroup of synapses has strongly diminished release (KO altered), it can be expected that the PPF protocol preferentially samples the subgroup with higher release probability (KO aligned). It is tempting to speculate that the structural correlate of the increased PPF in RIM1α KO might be the large fraction of vesicles that are both tethered and connected, which dominate the proximal zone in KO-aligned terminals (Fig. 5 D and Fig. S2), perhaps because of inadequate compensation by other RIMs. In this scenario, the release of one of these vesicles would pull its connected partners toward the AZ into a position where it can be easily released upon a second stimulus, thus leading to facilitation.

The increase in vesicle diameter in all KO synapses (Fig. S3) is another manifestation of the alterations beyond the AZ induced by the lack of RIM1α. Proteasome inhibition caused a significant increase in vesicle diameter both in WT and KO terminals, suggesting that the mechanisms of vesicle size control are also UPS dependent. Several scenarios could explain this phenomenon, from accumulation of nondegraded proteins on the vesicle membrane to alterations in the endocytic machinery leading to perturbed vesicle biogenesis (Edwards, 2007). In sum, our results not only provide a structural mechanism for the release defects observed in RIM1α KO terminals, but they also underscore the importance of the tethering machinery in vesicle exocytosis and point to the UPS as a novel regulator of presynaptic architecture.

Materials and methods

Synaptosomal preparation

RIM1α$^{-/-}$ mice were derived in a hybrid SV129/Bl6 background and subjected to at least four backcrosses into c57/Bl6 (Schoch et al., 2002). Cerebrocortical synaptosomes were extracted from 6–8-wk-old male RIM1α$^{+/+}$ and RIM1α$^{-/-}$ mice as previously described in Dunkley et al. (1988) and Godino et al. (2007) and in accordance with procedures accepted by the Max Planck Institute for Biochemistry. In brief, euthanized animals were decapitated, and the cerebral cortex was extracted and homogenized in homogenization buffer (HB; 0.32 M sucrose and 50 mM EDTA, pH 7.4) with up to seven strokes at 700 rpm in a Teflon glass homogenizer. The homogenate was centrifuged for 2 min at 2,000 *g*, and the pellet was resuspended in HB and centrifuged for another 2 min at 2,000 *g*. Supernatants from both centrifugations were combined and centrifuged for 12 min at 9,500 *g*. The pellet was resuspended in HB and loaded onto a three-step (3, 10, and 23%) Percoll (GE Healthcare) gradient in HB. The gradients were spun for 6 min at 25,000 *g*, and the material accumulated at the 10/23% interface was recovered and diluted to a final volume of 50 ml in Hepes-buffered medium (HBM; mM: 140 NaCl, 5 KCl, 5 $NaHCO_3$, 1.2 Na_2HPO_4, 1 $MgCl_2$, 10 glucose, and 10 Hepes, pH 7.4). Percoll was removed by centrifugation for 10 min at 22,000 *g*, and the pellet was resuspended in HBM supplemented with 1.2 mM $CaCl_2$ and immediately used in the experiments. All steps were performed at 4°C. No protease inhibitors were used during synaptosome preparation.

Synaptosomes were diluted to ∼1 mg/ml protein concentration determined by Bradford assay (Bio-Rad Laboratories) and preincubated for 30 min at 37°C. Before vitrification, synaptosomes were incubated for another 30 min at 37°C: without any additions, with 10 µM MG132 (carbobenzoyl-L-leucyl-L-leucyl-L-leucinal; Enzo Life Sciences) diluted in DMSO or with an equivalent amount of DMSO. Proteasome activity assays and Western blotting analysis were performed in DMSO- and MG132-treated synaptosomes only. Tomograms of untreated and DMSO-treated synaptosomes revealed no substantial differences and were pooled as control category. Only tomograms of synaptosomes containing mitochondria were selected for further analysis to ensure their viability (Harrison et al., 1988).

Vitrification

A 3-µl drop of 10-nm BSA-coated colloidal gold dissolved in PBS (Aurion) was deposited on plasma-cleaned, holey carbon copper EM grids (Quantifoil) and allowed to dry. A 3-µl drop of synaptosomal suspension was placed onto the grid, allowed to equilibrate for 5 s, blotted with filter paper (Whatman Grade 1), and plunged into a liquid ethane/propane mixture. Vitrified grids were stored in liquid nitrogen before imaging. No substantial diffusion of solutes from the dried gold solution into the synaptosomal suspension occurred, as Na^+ concentration increased to 160 ± 20 mM (mean ± SD, n = 9), when a 3-µl drop containing 140 mM NaCl was added to grids in which the gold solution was previously dried, and to 151 ± 2 mM (mean ± SD, n = 9), when using grids without dried gold solution (control). In both cases, the added drops were allowed to equilibrate on the grids for 30 s. The Na^+ concentration was determined by adding 10 µM CoroNa Green (Invitrogen) and monitoring the fluorescence on a fluorospectrometer (NanoDrop 3300; Thermo Fisher Scientific).

Proteasome activity assay

The synthetic fluorogenic peptide Suc-LLVY–7-amino-4-methylcoumarin (AMC; chymotryptic-like; Bachem) was used as a substrate to measure proteasomal activity (Kisselev and Goldberg, 2005). Fluorescence was measured at 37°C using a spectrophotometer (FLUOstar Optima; BMG LabTech). 20 µg synaptosomes was added to 150 µl HBM buffer. The reaction was initiated by the addition of Suc-LLVY-AMC substrate solution, resulting in a final concentration of 10 µM Suc-LLVY-AMC in a total final volume of 200 µl. Fluorescence of the reaction mixture was assayed immediately. The relative fluorescence was measured using excitation and emission wavelengths of 320 and 460 nm, respectively. Sample size was three pairs of WT and RIM1α KO littermates.

Western blotting

Synaptosomes from WT and RIM1α KO mice were treated with DMSO or MG132, mixed with 5× SDS sample buffer, and boiled. Samples were subjected to gel electrophoresis using a NuPAGE 4–12% Bis-Tris gel in MES SDS running buffer followed by immunoblotting. Mouse antibodies against RIM1 (610907) and MUNC13 (610999) were purchased from BD, Rab3 (107011), syntaxin1 (110011), SNAP25 (111002), VAMP2 (104211), and ELKS (143003) were purchased from Synaptic Systems, synaptotagmin1 (136088) and ubiquitin (8017) were obtained from Santa Cruz Biotechnology, Inc., α-tubulin (T6199) was obtained from Sigma-Aldrich, RIM2 was a gift from F. Schmitz (University of Saarland, Homberg, Germany), and Liprin2 and Liprin3 were obtained as previously described in Zürner et al. (2011). Protein expression was detected by the luminescent image analyzer (LAS-3000) and Image Reader LAS-3000 software (Leica). Sample size was 13 pairs of WT and RIM1α KO littermates.

Immunofluorescence imaging

Synaptosomes from WT and RIM1α KO mice were treated with DMSO or MG132 and processed as previously described (Martín et al., 2007). In brief, synaptosomes were plated on poly-L-lysine–coated coverslips and allowed to attach for 30 min followed by 30-min incubation with DMSO or MG132. Synaptosomes were fixed for 5 min in PBS containing 4% paraformaldehyde and blocked with PBS containing 1% BSA, 10% normal goat serum, and 0.1% Triton X-100. After several washes, synaptosomes were incubated with primary antibodies for 12–14 h (antibodies for RIM1 and RIM2 were a gift from F. Schmitz; MUNC13 [126102], VAMP2 [104211], and ELKS [143003] antibodies were purchased from Synaptic Systems; and the Bassoon [SAP7F407] antibody was purchased from Enzo Life Sciences). Synaptosomes were washed and further incubated with secondary antibodies for 40 min at room temperature (goat anti–mouse FITC and goat anti–rabbit Cy3 were purchased from Jackson ImmunoResearch Laboratories, Inc.). Coverslips were washed extensively in PBS and mounted in Mowiol (Sigma-Aldrich). Images were acquired at room temperature in a laser-scanning confocal microscope (A1; Nikon) using a CFI Plan Apochromat infrared 60× water immersion objective (NA 1.27) and NIS-Elements 4.0 acquisition software (Nikon). The fraction of AZ protein staining (ELKS, MUNC13, RIM1, and RIM2) colocalizing with presynaptic marker staining (VAMP2 and Bassoon) was quantified using thresholded Manders' coefficients as implemented in the JACoP plugin (Bolte and Cordelières, 2006) of ImageJ (National Institutes of Health; Schneider et al., 2012). Sample size was five pairs of WT and RIM1α KO littermates, with 15–20 images per condition.

Electrophysiological recordings

Synaptic responses were recorded from hippocampal slices (400 µm) of 2–3-wk-old mice at room temperature by extracellular field potentials (fEPSPs) in the stratum radiatum in CA1. Slices were stored and recorded in artificial cerebrospinal fluid (ACSF) containing the following (mM): 130 NaCl, 2.75 KCl, 1.5 $MgSO_4$, 2.5 $CaCl_2$, 1.1 $NaHPO_4$, 28.82 $NaHCO_3$, and 11 glucose saturated with 95% O_2 and 5% CO_2, pH 7.4. A subset of slices was preincubated in ACSF containing 10 µM MG132 for 1–2 h. Recording and stimulation pipettes were filled with ACSF. Schaffer collaterals were stimulated at 0.1 Hz, and initial slopes of fEPSPs were measured. PPF was evoked by a second stimulus 40 ms after the first stimulus. All data were acquired on littermate offspring from heterozygous matings and analyzed without knowledge of the genotype of the tissue being studied. Sample sizes (slices/animals) are as follows: WT, 14/4; WT + MG132, 16/4; RIM1α KO, 14/4; and RIM1α KO + MG132, 13/4.

Cryo-ET

Tilt series were collected under a low dose acquisition scheme using an electron microscope (Polara; FEI) operated at 300 kV. The microscope was equipped with a field emission gun, a 2,048 × 2,048 charge-coupled device camera (MultiScan; Gatan), a postcolumn energy filter (Gatan) operated in the zero-loss mode, and a computerized cryostage designed to maintain the specimen temperature below −150°C. Tilt series were recorded using Xplore3D (FEI), typically from −60° to 60° with 2° angular increment. Pixel size was 0.66 nm at the specimen level, and the defocus was set to −9 µm. The total dose was kept below 150 $e^-/Å^2$.

Tilt series were aligned using gold beads as fiducial markers, and 3D reconstructions were obtained by weighted back projection with analytical weighting using the TOM toolbox (Nickell et al., 2005). During reconstruction, the projections were binned twice (final voxel size of 2.64 nm) and low pass filtered at the postbinning Nyquist frequency, thus limiting the nominal tomogram resolution of the tomograms to the voxel size. The tomograms were subsequently denoised by anisotropic nonlinear diffusion filtering (Fernández and Li, 2003). 5.4-nm-thick tomographic images shown in Fig. 1 and Fig. 7 were formed by addition of two consecutive 2.64-nm-thick slices. Tomographic slices are displayed using the interpolation tool of IMOD (Kremer et al., 1996).

Image segmentation

The AZ was manually segmented in Amira (Visualization Sciences Group). A maximum diameter profile along the z axis was manually traced for all synaptic vesicles within 250 nm from the AZ and subsequently substituted with a sphere of the same diameter and center. The elements of the presynaptic cytomatrix were segmented automatically using a Pyto package combining the watershed transform and connectivity-based segmentation (Fernández-Busnadiego et al., 2010). Only filaments contacting exactly two vesicles (connectors) or one vesicle and the AZ (tethers) were analyzed because these were the most prominent filament types found by visual inspection. The morphological properties, location parameters, and grayscale values were determined for all synaptic vesicles, tethers, and connectors of each synapse separately. For the analysis of vesicle distribution, the part of the interior of the presynaptic terminal occupied by synaptic vesicles was divided into 1-pixel-thick layers according to the distance to the AZ, and the fraction of layer volume occupied by vesicles was measured. In cases involving vesicle distance to the AZ, the distance of the vesicle center to the AZ was used. All parameters were analyzed only within 250 nm from the AZ. Connector and tether lengths were estimated from the positions of contact voxels (voxels that contact the vesicle membrane or the AZ). Consequently, connector and tether lengths calculated membrane to membrane would be ∼1 pixel (2.64 nm) longer. All software procedures were written in Python using NumPy and SciPy packages.

Statistical analysis

For the analysis of connectivity, tethering, and vesicle diameter and distribution, values calculated for each category of samples were combined and statistically analyzed. The numbers of vesicles, connectors, and tethers analyzed for each category are shown in Table S1. Averages were calculated over all measurements of a specific property. We used *t* test for statistical analysis of values that appeared to be normally distributed (e.g., vesicle diameter) and K-W test (nonparametric) for values deviating from the normal distribution (e.g., number of tethers/connectors per vesicle). When values fell into discrete bins (e.g., fraction of connected and nonconnected vesicles), the χ^2 test was used. We used Pearson's coefficient for correlation analysis, and its significance was determined using *t* test. In all cases, confidence levels were calculated using two-tailed tests. The confidence values were indicated in the graphs by a single asterisk for $P < 0.05$, a double asterisk for $P < 0.01$, and a triple asterisk for $P < 0.001$.

Online supplemental material

Fig. S1 shows synaptosomes immunostained for different presynaptic proteins. Fig. S2 displays a semiquantitative summary of tethering, connectivity, and vesicle size data for proximal vesicles. Fig. S3 shows synaptic vesicle diameter for vesicles within 250 nm from the AZ. Fig. S4 shows proteasome chymotryptic-like activity in synaptosomes. Table S1 summarizes the number of animals, synapses, synaptic vesicles, connectors, and tethers analyzed for each category are summarized. Video 1, Video 2, and Video 3 show tomograms and the corresponding 3D renderings of WT, RIM1α KO-altered, and RIM1α KO-aligned synapses, respectively. A ZIP file is also provided that contains a code that was used to perform statistical analysis of the segmentation results and plot all graphs shown in this paper. Online supplemental material is available at http://www.jcb.org/cgi/content/full/jcb.201206063/DC1.

We would like to thank Verena Borm for technical assistance and Xinran Liu, Mirko Messa, and Ira Milosevic for critical reading of the manuscript.

This work was supported by grants from the Deutsche Forschungsgemeinschaft (SFB/TR3 and SFB645), the Bundesministeriums für Bildung und Forschung (Nationale Genomforschungsnetz-Netzwerk Epilepsie und Migräne and Unabhängige Forschergruppen in den Neurowissenschaften), and BONFOR. R. Fernández-Busnadiego is recipient of a Feodor-Lynen Fellowship from the Alexander von Humboldt Foundation, and thanks Pietro de Camilli for support.

Submitted: 15 June 2012
Accepted: 11 April 2013

References

Andrews-Zwilling, Y.S., H. Kawabe, K. Reim, F. Varoqueaux, and N. Brose. 2006. Binding to Rab3A-interacting molecule RIM regulates the presynaptic recruitment of Munc13-1 and ubMunc13-2. *J. Biol. Chem.* 281: 19720–19731. http://dx.doi.org/10.1074/jbc.M601421200

Aravamudan, B., and K. Broadie. 2003. Synaptic *Drosophila* UNC-13 is regulated by antagonistic G-protein pathways via a proteasome-dependent degradation mechanism. *J. Neurobiol.* 54:417–438. http://dx.doi.org/10.1002/neu.10142

Bingol, B., and M. Sheng. 2011. Deconstruction for reconstruction: the role of proteolysis in neural plasticity and disease. *Neuron.* 69:22–32. http://dx.doi.org/10.1016/j.neuron.2010.11.006

Blundell, J., P.S. Kaeser, T.C. Südhof, and C.M. Powell. 2010. RIM1α and interacting proteins involved in presynaptic plasticity mediate prepulse inhibition and additional behaviors linked to schizophrenia. *J. Neurosci.* 30:5326–5333. http://dx.doi.org/10.1523/JNEUROSCI.0328-10.2010

Bolte, S., and F.P. Cordelières. 2006. A guided tour into subcellular colocalization analysis in light microscopy. *J. Microsc.* 224:213–232. http://dx.doi.org/10.1111/j.1365-2818.2006.01706.x

Calakos, N., S. Schoch, T.C. Südhof, and R.C. Malenka. 2004. Multiple roles for the active zone protein RIM1α in late stages of neurotransmitter release. *Neuron*. 42:889–896. http://dx.doi.org/10.1016/j.neuron.2004.05.014

Dani, A., B. Huang, J. Bergan, C. Dulac, and X. Zhuang. 2010. Superresolution imaging of chemical synapses in the brain. *Neuron*. 68:843–856. http://dx.doi.org/10.1016/j.neuron.2010.11.021

Deng, L., P.S. Kaeser, W. Xu, and T.C. Südhof. 2011. RIM proteins activate vesicle priming by reversing autoinhibitory homodimerization of Munc13. *Neuron*. 69:317–331. http://dx.doi.org/10.1016/j.neuron.2011.01.005

de Wit, H., A.M. Walter, I. Milosevic, A. Gulyás-Kovács, D. Riedel, J.B. Sørensen, and M. Verhage. 2009. Synaptotagmin-1 docks secretory vesicles to syntaxin-1/SNAP-25 acceptor complexes. *Cell*. 138:935–946. http://dx.doi.org/10.1016/j.cell.2009.07.027

Dubochet, J., and N. Sartori Blanc. 2001. The cell in absence of aggregation artifacts. *Micron*. 32:91–99. http://dx.doi.org/10.1016/S0968-4328(00)00026-3

Dubochet, J., M. Adrian, J.-J. Chang, J.-C. Homo, J. Lepault, A.W. McDowall, and P. Schultz. 1988. Cryo-electron microscopy of vitrified specimens. *Q. Rev. Biophys.* 21:129–228. http://dx.doi.org/10.1017/S0033583500004297

Dunkley, P.R., J.W. Heath, S.M. Harrison, P.E. Jarvie, P.J. Glenfield, and J.A.P. Rostas. 1988. A rapid Percoll gradient procedure for isolation of synaptosomes directly from an S1 fraction: homogeneity and morphology of subcellular fractions. *Brain Res.* 441:59–71. http://dx.doi.org/10.1016/0006-8993(88)91383-2

Edwards, R.H. 2007. The neurotransmitter cycle and quantal size. *Neuron*. 55:835–858. http://dx.doi.org/10.1016/j.neuron.2007.09.001

Fernández, J.-J., and S. Li. 2003. An improved algorithm for anisotropic nonlinear diffusion for denoising cryo-tomograms. *J. Struct. Biol.* 144:152–161. http://dx.doi.org/10.1016/j.jsb.2003.09.010

Fernández-Busnadiego, R., B. Zuber, U.E. Maurer, M. Cyrklaff, W. Baumeister, and V. Lučić. 2010. Quantitative analysis of the native presynaptic cytomatrix by cryoelectron tomography. *J. Cell Biol.* 188:145–156. http://dx.doi.org/10.1083/jcb.200908082

Fernández-Busnadiego, R., N. Schrod, Z. Kochovski, S. Asano, D. Vanhecke, W. Baumeister, and V. Lučić. 2011. Insights into the molecular organization of the neuron by cryo-electron tomography. *J. Electron Microsc. (Tokyo)*. 60(Suppl. 1):S137–S148. http://dx.doi.org/10.1093/jmicro/dfr018

Fioravante, D., R.-Y. Liu, and J.H. Byrne. 2008. The ubiquitin-proteasome system is necessary for long-term synaptic depression in *Aplysia*. *J. Neurosci.* 28:10245–10256. http://dx.doi.org/10.1523/JNEUROSCI.2139-08.2008

Godino, MdelC., M. Torres, and J. Sánchez-Prieto. 2007. CB1 receptors diminish both Ca^{2+} influx and glutamate release through two different mechanisms active in distinct populations of cerebrocortical nerve terminals. *J. Neurochem.* 101:1471–1482. http://dx.doi.org/10.1111/j.1471-4159.2006.04422.x

Hallermann, S., A. Fejtova, H. Schmidt, A. Weyhersmüller, R.A. Silver, E.D. Gundelfinger, and J. Eilers. 2010a. Bassoon speeds vesicle reloading at a central excitatory synapse. *Neuron*. 68:710–723. http://dx.doi.org/10.1016/j.neuron.2010.10.026

Hallermann, S., R.J. Kittel, C. Wichmann, A. Weyhersmüller, W. Fouquet, S. Mertel, D. Owald, S. Eimer, H. Depner, M. Schwärzel, et al. 2010b. Naked dense bodies provoke depression. *J. Neurosci.* 30:14340–14345. http://dx.doi.org/10.1523/JNEUROSCI.2495-10.2010

Han, Y., P.S. Kaeser, T.C. Südhof, and R. Schneggenburger. 2011. RIM determines Ca^{2+} channel density and vesicle docking at the presynaptic active zone. *Neuron*. 69:304–316. http://dx.doi.org/10.1016/j.neuron.2010.12.014

Harrison, S.M., P.E. Jarvie, and P.R. Dunkley. 1988. A rapid Percoll gradient procedure for isolation of synaptosomes directly from an S1 fraction: viability of subcellular fractions. *Brain Res.* 441:72–80. http://dx.doi.org/10.1016/0006-8993(88)91384-4

Hirokawa, N., K. Sobue, K. Kanda, A. Harada, and H. Yorifuji. 1989. The cytoskeletal architecture of the presynaptic terminal and molecular structure of synapsin 1. *J. Cell Biol.* 108:111–126. http://dx.doi.org/10.1083/jcb.108.1.111

Jahn, R., and D. Fasshauer. 2012. Molecular machines governing exocytosis of synaptic vesicles. *Nature*. 490:201–207. http://dx.doi.org/10.1038/nature11320

Jiang, X., P.E. Litkowski, A.A. Taylor, Y. Lin, B.J. Snider, and K.L. Moulder. 2010. A role for the ubiquitin-proteasome system in activity-dependent presynaptic silencing. *J. Neurosci.* 30:1798–1809. http://dx.doi.org/10.1523/JNEUROSCI.4965-09.2010

Kaeser, P.S., H.-B. Kwon, C.Q. Chiu, L. Deng, P.E. Castillo, and T.C. Südhof. 2008. RIM1α and RIM1β are synthesized from distinct promoters of the RIM1 gene to mediate differential but overlapping synaptic functions. *J. Neurosci.* 28:13435–13447. http://dx.doi.org/10.1523/JNEUROSCI.3235-08.2008

Kaeser, P.S., L. Deng, Y. Wang, I. Dulubova, X. Liu, J. Rizo, and T.C. Südhof. 2011. RIM proteins tether Ca2+ channels to presynaptic active zones via a direct PDZ-domain interaction. *Cell*. 144:282–295. http://dx.doi.org/10.1016/j.cell.2010.12.029

Kalla, S., M. Stern, J. Basu, F. Varoqueaux, K. Reim, C. Rosenmund, N.E. Ziv, and N. Brose. 2006. Molecular dynamics of a presynaptic active zone protein studied in Munc13-1-enhanced yellow fluorescent protein knock-in mutant mice. *J. Neurosci.* 26:13054–13066. http://dx.doi.org/10.1523/JNEUROSCI.4330-06.2006

Kisselev, A.F., and A.L. Goldberg. 2005. Monitoring activity and inhibition of 26S proteasomes with fluorogenic peptide substrates. *Methods Enzymol.* 398:364–378. http://dx.doi.org/10.1016/S0076-6879(05)98030-0

Kremer, J.R., D.N. Mastronarde, and J.R. McIntosh. 1996. Computer visualization of three-dimensional image data using IMOD. *J. Struct. Biol.* 116:71–76. http://dx.doi.org/10.1006/jsbi.1996.0013

Landis, D.M.D., A.K. Hall, L.A. Weinstein, and T.S. Reese. 1988. The organization of cytoplasm at the presynaptic active zone of a central nervous system synapse. *Neuron*. 1:201–209. http://dx.doi.org/10.1016/0896-6273(88)90140-7

Lazarevic, V., C. Schöne, M. Heine, E.D. Gundelfinger, and A. Fejtova. 2011. Extensive remodeling of the presynaptic cytomatrix upon homeostatic adaptation to network activity silencing. *J. Neurosci.* 31:10189–10200. http://dx.doi.org/10.1523/JNEUROSCI.2088-11.2011

Li, F., F. Pincet, E. Perez, W.S. Eng, T.J. Melia, J.E. Rothman, and D. Tareste. 2007. Energetics and dynamics of SNAREpin folding across lipid bilayers. *Nat. Struct. Mol. Biol.* 14:890–896. http://dx.doi.org/10.1038/nsmb1310

Li, W., C. Ma, R. Guan, Y. Xu, D.R. Tomchick, and J. Rizo. 2011. The crystal structure of a Munc13 C-terminal module exhibits a remarkable similarity to vesicle tethering factors. *Structure*. 19:1443–1455. http://dx.doi.org/10.1016/j.str.2011.07.012

Ma, C., W. Li, Y. Xu, and J. Rizo. 2011. Munc13 mediates the transition from the closed syntaxin-Munc18 complex to the SNARE complex. *Nat. Struct. Mol. Biol.* 18:542–549. http://dx.doi.org/10.1038/nsmb.2047

Ma, C., L. Su, A.B. Seven, Y. Xu, and J. Rizo. 2013. Reconstitution of the vital functions of Munc18 and Munc13 in neurotransmitter release. *Science*. 339:421–425. http://dx.doi.org/10.1126/science.1230473

Martín, R., M. Torres, and J. Sánchez-Prieto. 2007. mGluR7 inhibits glutamate release through a PKC-independent decrease in the activity of P/Q-type Ca2+ channels and by diminishing cAMP in hippocampal nerve terminals. *Eur. J. Neurosci.* 26:312–322. http://dx.doi.org/10.1111/j.1460-9568.2007.05660.x

Mittelstaedt, T., E. Alvaréz-Baron, and S. Schoch. 2010. RIM proteins and their role in synapse function. *Biol. Chem.* 391:599–606. http://dx.doi.org/10.1515/bc.2010.064

Mukherjee, K., X. Yang, S.H. Gerber, H.-B. Kwon, A. Ho, P.E. Castillo, X. Liu, and T.C. Südhof. 2010. Piccolo and bassoon maintain synaptic vesicle clustering without directly participating in vesicle exocytosis. *Proc. Natl. Acad. Sci. USA*. 107:6504–6509. http://dx.doi.org/10.1073/pnas.1002307107

Nicholls, D.G. 2003. Bioenergetics and transmitter release in the isolated nerve terminal. *Neurochem. Res.* 28:1433–1441. http://dx.doi.org/10.1023/A:1025653805029

Nickell, S., F. Förster, A. Linaroudis, W.D. Net, F. Beck, R. Hegerl, W. Baumeister, and J.M. Plitzko. 2005. TOM software toolbox: acquisition and analysis for electron tomography. *J. Struct. Biol.* 149:227–234. http://dx.doi.org/10.1016/j.jsb.2004.10.006

Pitsch, J., T. Opitz, V. Borm, A. Woitecki, M. Staniek, H. Beck, A.J. Becker, and S. Schoch. 2012. The presynaptic active zone protein RIM1α controls epileptogenesis following status epilepticus. *J. Neurosci.* 32:12384–12395. http://dx.doi.org/10.1523/JNEUROSCI.0223-12.2012

Powell, C.M., S. Schoch, L. Monteggia, M. Barrot, M.F. Matos, N. Feldmann, T.C. Südhof, and E.J. Nestler. 2004. The presynaptic active zone protein RIM1α is critical for normal learning and memory. *Neuron*. 42:143–153. http://dx.doi.org/10.1016/S0896-6273(04)00146-1

Rinetti, G.V., and F.E. Schweizer. 2010. Ubiquitination acutely regulates presynaptic neurotransmitter release in mammalian neurons. *J. Neurosci.* 30:3157–3166. http://dx.doi.org/10.1523/JNEUROSCI.3712-09.2010

Schikorski, T., and C.F. Stevens. 1997. Quantitative ultrastructural analysis of hippocampal excitatory synapses. *J. Neurosci.* 17:5858–5867.

Schneider, C.A., W.S. Rasband, and K.W. Eliceiri. 2012. NIH Image to ImageJ: 25 years of image analysis. *Nat. Methods*. 9:671–675. http://dx.doi.org/10.1038/nmeth.2089

Schoch, S., and E.D. Gundelfinger. 2006. Molecular organization of the presynaptic active zone. *Cell Tissue Res.* 326:379–391. http://dx.doi.org/10.1007/s00441-006-0244-y

Schoch, S., P.E. Castillo, T. Jo, K. Mukherjee, M. Geppert, Y. Wang, F. Schmitz, R.C. Malenka, and T.C. Südhof. 2002. RIM1α forms a protein scaffold for regulating neurotransmitter release at the active zone. *Nature*. 415:321–326. http://dx.doi.org/10.1038/415321a

Schoch, S., T. Mittelstaedt, P.S. Kaeser, D. Padgett, N. Feldmann, V. Chevaleyre, P.E. Castillo, R.E. Hammer, W. Han, F. Schmitz, et al. 2006. Redundant functions of RIM1α and RIM2α in Ca(2+)-triggered neurotransmitter release. *EMBO J.* 25:5852–5863. http://dx.doi.org/10.1038/sj.emboj.7601425

Siksou, L., P. Rostaing, J.-P. Lechaire, T. Boudier, T. Ohtsuka, A. Fejtová, H.-T. Kao, P. Greengard, E.D. Gundelfinger, A. Triller, and S. Marty. 2007. Three-dimensional architecture of presynaptic terminal cytomatrix. *J. Neurosci.* 27:6868–6877. http://dx.doi.org/10.1523/JNEUROSCI.1773-07.2007

Siksou, L., F. Varoqueaux, O. Pascual, A. Triller, N. Brose, and S. Marty. 2009. A common molecular basis for membrane docking and functional priming of synaptic vesicles. *Eur. J. Neurosci.* 30:49–56. http://dx.doi.org/10.1111/j.1460-9568.2009.06811.x

Siksou, L., A. Triller, and S. Marty. 2011. Ultrastructural organization of presynaptic terminals. *Curr. Opin. Neurobiol.* 21:261–268. http://dx.doi.org/10.1016/j.conb.2010.12.003

Speese, S.D., N. Trotta, C.K. Rodesch, B. Aravamudan, and K. Broadie. 2003. The ubiquitin proteasome system acutely regulates presynaptic protein turnover and synaptic efficacy. *Curr. Biol.* 13:899–910. http://dx.doi.org/10.1016/S0960-9822(03)00338-5

Südhof, T.C. 2004. The synaptic vesicle cycle. *Annu. Rev. Neurosci.* 27:509–547. http://dx.doi.org/10.1146/annurev.neuro.26.041002.131412

Südhof, T.C. 2012. The presynaptic active zone. *Neuron*. 75:11–25. http://dx.doi.org/10.1016/j.neuron.2012.06.012

Tada, H., H.J. Okano, H. Takagi, S. Shibata, I. Yao, M. Matsumoto, T. Saiga, K.I. Nakayama, H. Kashima, T. Takahashi, et al. 2010. Fbxo45, a novel ubiquitin ligase, regulates synaptic activity. *J. Biol. Chem.* 285:3840–3849. http://dx.doi.org/10.1074/jbc.M109.046284

Tai, H.-C., H. Besche, A.L. Goldberg, and E.M. Schuman. 2010. Characterization of the brain 26S proteasome and its interacting proteins. *Front Mol. Neurosci*. 3:12.

Tao-Cheng, J.H. 2006. Activity-related redistribution of presynaptic proteins at the active zone. *Neuroscience*. 141:1217–1224. http://dx.doi.org/10.1016/j.neuroscience.2006.04.061

Thomson, A.M. 2000. Facilitation, augmentation and potentiation at central synapses. *Trends Neurosci.* 23:305–312. http://dx.doi.org/10.1016/S0166-2236(00)01580-0

Upadhya, S.C., L. Ding, T.K. Smith, and A.N. Hegde. 2006. Differential regulation of proteasome activity in the nucleus and the synaptic terminals. *Neurochem. Int.* 48:296–305. http://dx.doi.org/10.1016/j.neuint.2005.11.003

van den Bogaart, G., S. Thutupalli, J.H. Risselada, K. Meyenberg, M. Holt, D. Riedel, U. Diederichsen, S. Herminghaus, H. Grubmüller, and R. Jahn. 2011. Synaptotagmin-1 may be a distance regulator acting upstream of SNARE nucleation. *Nat. Struct. Mol. Biol.* 18:805–812. http://dx.doi.org/10.1038/nsmb.2061

Vanhecke, D., S. Asano, Z. Kochovski, R. Fernández-Busnadiego, N. Schrod, W. Baumeister, and V. Lučić. 2011. Cryo-electron tomography: methodology, developments and biological applications. *J. Microsc.* 242:221–227. http://dx.doi.org/10.1111/j.1365-2818.2010.03478.x

Whittaker, V.P. 1993. Thirty years of synaptosome research. *J. Neurocytol.* 22:735–742. http://dx.doi.org/10.1007/BF01181319

Yao, I., H. Takagi, H. Ageta, T. Kahyo, S. Sato, K. Hatanaka, Y. Fukuda, T. Chiba, N. Morone, S. Yuasa, et al. 2007. SCRAPPER-dependent ubiquitination of active zone protein RIM1 regulates synaptic vesicle release. *Cell*. 130:943–957. http://dx.doi.org/10.1016/j.cell.2007.06.052

Zürner, M., T. Mittelstaedt, S. tom Dieck, A. Becker, and S. Schoch. 2011. Analyses of the spatiotemporal expression and subcellular localization of liprin-α proteins. *J. Comp. Neurol.* 519:3019–3039. http://dx.doi.org/10.1002/cne.22664